PHYSICAL REVIEW B **68**, 235327 (2003)

Optical transitions in a single CdTe spherical quantum dot

S. J. Prado,[1,*] C. Trallero-Giner,[2] A. M. Alcalde,[1] V. López-Richard,[3] and G. E. Marques[1]
[1]*Departamento de Física, UFSCar, Caixa Postal 676, 13565-905 São Carlos, São Paulo, Brazil*
[2]*Departament of Theoretical Physics, Havana University, Vedado 10400, Cuba*
[3]*Instituto de Física de São Carlos, USP, 13560-970 São Carlos, São Paulo, Brazil*

(Received 10 June 2002; revised manuscript received 4 June 2003; published 24 December 2003)

We discuss different aspects of the optical properties in a single CdTe spherical quantum dot after performing a systematic study of the eigenvalues, wave functions, and their dominant symmetries within the 8×8 $\mathbf{k}\cdot\mathbf{p}$ Kane-Weiler Hamiltonian derived from the conduction-valence band coupling and the mixing of the valence states. The analysis of the inherent symmetries in the Hamiltonian leads to basis function sets separated into two Hilbert subspaces. A detailed discussion of the symmetries associated with the electronic levels and the selection rules for optical transitions are derived by considering circular polarization for the incident light. We also calculated the optical oscillator strengths and the corresponding absorption spectra in the dipole approximation. Also, we discuss the roles of nonparabolicity, valence-band admixture, and symmetry signatures of the involved states. We compare the numerical results for the electronic dispersions in a zinc-blende based quantum dot when the spherical or the axial approximations are used inside the 8×8 multiband Hamiltonian.

DOI: 10.1103/PhysRevB.68.235327 PACS number(s): 73.21.La, 78.67.Hc

I. INTRODUCTION

Semiconductor quantum dots are new man-made crystalline systems exhibiting electronic and optical properties that cannot be observed in bulk materials. Due to the full quantization of all degrees of freedom the electronic spectrum of a single quantum dot, such as in atoms, always consists of a discrete set of eigenvalues and this is where lies its great interest from the point of view of fundamental physics and also for their potential application in microelectronic and optoelectronic devices such as light-emitting diodes. Much effort has been dedicated to understand as well as to explore the physical properties of these systems both theoretically and experimentally. In the present work we will define a quantum dot as a microsphere of radius R.

The quantum confined states and the optical transitions between these quasi-zero-dimensional states have been studied by several experimental techniques. The photoluminescence excitation experiments permit to study the evolution of the electronic spectra with respect to R.[1,2] The observation of persistent hole burning enabled the investigation of the size dependence of these electronic levels.[3] Additionally, important experimental and theoretical results on the optical properties of quantum dots have been compiled by Woggon.[4] Recently, new optical properties were discovered in quantum dots as, for instance, the photostimulated luminescence observed by Masumoto[5] in spherical quantum dots (SQD's). The understanding and interpretation of these experimental results would require a proper and precise description of the optical selection rules, a study of the dependence of the energy levels on the dot size and on the spatial symmetry as well as the effects of external fields on the electronic states of these atomiclike systems. These components are strongly affected and mutually connected by the quantum confinement. Therefore, an extended theoretical work is needed to explain the different aspects of the electronic transitions and symmetries of the involved states.

If compared to CdS and CdSe quantum dots, the CdTe microcrystallites imbedded in a host matrix are better suited for the study of the strong confinement regime, where the individual motions of electrons and holes are restricted to the size quantization region. This limit is realized when the bulk exciton Bohr radius a_B exceeds significantly the quantum dot radius and, thus, the Coulomb interaction between the electron-hole pairs can be considered as negligible.

The assignment of the electronic states based on the multiband effective-mass theory has provided strong foundations for description of the electronic structure in quantum dots.[1,2] The properties derived from it have helped the analysis of different results, such as the optical absorption,[6] the resonant tunneling of holes,[7] the g-factor evaluation[8] in layered heterostructures, and the Raman-scattering processes under applied magnetic fields in bulk zinc-blende semiconductors.[9]

Several versions of this theory under different approximations have been formulated from bulk materials to zinc-blende[10–14] and wurtzite[15] based nanostructures. Here we have chosen to use the 8×8 $\mathbf{k}\cdot\mathbf{p}$ Kane-Weiler model,[16–18] to study all different aspects of the interaction between the Γ_6, Γ_8, and Γ_7 bands as well as the symmetries imposed to the involved states in SQD's under strong confinement regime. Besides, the influences of these band interactions on their optical selection rules are yet scarce and a more complete theory should be desired to provide better understanding of their electronic structure and optical spectra. A remarkable effort has been done by Sercel[13] and by Efros[10] to study the electronic states in SQD's under different approaches. In order to achieve analytical expressions for the radial part of the wave functions and eigenenergies, Ref. 10 has assumed the spherical eight-band model and Refs. 11 and 14 have implemented a simplified block-diagonalized 4×4 Hamiltonian model. Several II-VI and III-V semiconductor compounds present zinc-blende symmetry where the Luttinger parameters γ_1, γ_2, and γ_3 are different. By neglecting the warping term $\mu=(\gamma_2-\gamma_3)/2$ and considering $\gamma_2\neq\gamma_3$ except where the μ terms occur, the $\mathbf{k}\cdot\mathbf{p}$ Hamiltonian is reduced to the well-known axial approximation.[18]

In the present work we have implemented the 8×8 Kane-Weiler Hamiltonian beyond the spherical approximation for zinc-blende based nanostructures to study the size and SQD parameter dependences and the general nature of the electronic states. We present an extensive theoretical study of the eigenvalues, the dominant symmetries in the Hilbert space for a single CdTe SQD. In the following section we present results from a rigorous calculation of the electronic wave functions and energy eigenvalues within the $\mathbf{k}\cdot\mathbf{p}$ Hamiltonian model. We also have derived the selection rules and calculated the interband optical oscillator strengths and the absorption coefficients for circular polarization in single dots. The general discussions are presented in Sec. III and, finally, Sec. IV is devoted to our conclusions.

II. THEORY

A. Symmetry of k·p states of spherical quantum dots

Electron and hole states in SQD can be characterized by eigenstates of the *z* component of the total angular momentum defined by the sum of the Bloch, **J**, and the envelope, **L**, angular momenta, respectively. Within the 8×8 $\mathbf{k}\cdot\mathbf{p}$ model, these states can be written as a linear expansion in the form of eight-component spinor functions. The Hamiltonian model is shown in the Appendix [see Eq. (A2)].

Several remarks should be made regarding our version of the method when applied to SQD's:

(i) We shall assume an infinite barrier confining model.

(ii) As stated in Sec. I in reality we can define here two types of $\mathbf{k}\cdot\mathbf{p}$ Hamiltonians to study the electronic levels in SQD's: (a) One is the spherical model where we assume $\gamma_2=\gamma_3$ in every term; (b) another is the axial model where we let $\bar{\gamma}=(2\gamma_2+3\gamma_3)/5$ and $\gamma_2\neq\gamma_3$ everywhere but in the terms proportional to μ which are set to zero. In the case of the axial model diagonal (A3) and off-diagonal (A4) elements in the Hamiltonian (A2) present different inversion symmetries and the structure of operators (A2) determine an inherent symmetry that allows the separation of the Hilbert space into two orthogonal subspaces. To satisfy the inversion symmetry of the diagonal and off-diagonal operators in our Hamiltonian, each subspace must be formed by special combination of even and odd states [see below Eqs. (1) and (2)].

(iii) In both Hamiltonian models the *z* component of the orbital angular momentum $L_z=\hbar M$ of the envelope wave function remains as a good quantum number. The wave functions for any electronic state are represented by an eight-component spinor. A complete set of eigenfunctions for the $\mathbf{k}\cdot\mathbf{p}$ Hamiltonian of the spherical QD can be expanded in terms of the product of the periodic Bloch functions $|J,J_z\rangle$ at $k=0$ and envelope functions. In order to take full advantage of the above-mentioned symmetry properties, we shall expand the eight-component spinor wave functions in each Hilbert subspace, in terms of the exact solutions of the diagonal terms for each carrier type. Each component of the spinor has the form $f^M_{n,L}(\mathbf{r})=A_{n,L}j_L(k^L_n r)Y^M_L(\theta,\phi)$ (Ref. 19), where $A_{n,L}$ is a normalization constant, $j_L(x)$ is the spherical Bessel function, and $Y^M_L(\theta,\phi)$ the spherical harmonics. If we neglect the warping term, each subspace can be constructed with a special combination of even, $f^M_{n,2L}(\mathbf{r})$, and odd, $f^M_{n,2L+1}(r)$functions. The general forms of the spinor states are given by

$$|\psi^M_{\mathrm{I}}(\mathbf{r})\rangle=\sum_n\sum_{L\geqslant|M|}\begin{pmatrix} C^M_{n,2L}f^M_{n,2L}(\mathbf{r})|e^+\rangle\\ C^{M-1}_{n,2L+1}f^{M-1}_{n,2L+1}(\mathbf{r})|hh^+\rangle\\ C^M_{n,2L+1}f^M_{n,2L+1}(\mathbf{r})|lh^+\rangle\\ C^M_{n,2L+1}f^M_{n,2L+1}(\mathbf{r})|so^+\rangle\\ C^{M+1}_{n,2L}f^{M+1}_{n,2L}(\mathbf{r})|e^-\rangle\\ C^{M+2}_{n,2L+1}f^{M+2}_{n,2L+1}(\mathbf{r})|hh^-\rangle\\ C^{M+1}_{n,2L+1}f^{M+1}_{n,2L+1}(\mathbf{r})|lh^-\rangle\\ C^{M+1}_{n,2L+1}f^{M+1}_{n,2L+1}(\mathbf{r})|so^-\rangle \end{pmatrix} \tag{1}$$

and

$$|\psi^M_{\mathrm{II}}(\mathbf{r})\rangle=\sum_n\sum_{L\geqslant|M|}\begin{pmatrix} C^M_{n,2L+1}f^M_{n,2L+1}(\mathbf{r})|e^+\rangle\\ C^{M-1}_{n,2L}f^{M-1}_{n,2L}(\mathbf{r})|hh^+\rangle\\ C^M_{n,2L}f^M_{n,2L}(\mathbf{r})|lh^+\rangle\\ C^M_{n,2L}f^M_{n,2L}(\mathbf{r})|so^+\rangle\\ C^{M+1}_{n,2L+1}f^{M+1}_{n,2L+1}(\mathbf{r})|e^-\rangle\\ C^{M+2}_{n,2L}f^{M+2}_{n,2L}(\mathbf{r})|hh^-\rangle\\ C^{M+1}_{n,2L}f^{M+1}_{n,2L}(\mathbf{r})|lh^-\rangle\\ C^{M+1}_{n,2L}f^{M+1}_{n,2L}(\mathbf{r})|so^-\rangle \end{pmatrix}, \tag{2}$$

where $C^M_{n,L}$ are constants to be determined. It is important to remark that the above states are in the *L*-*J* coupling scheme, where the eigenstates are obtained by an expansion in a basis of wave functions with well defined projection $\hbar F_z$ ($F_z=\pm1/2,\pm3/2,\dots$) of the total angular momentum $F=L+J$. The special order of the number *M* in wave functions (1) and (2) is dictated by the constant of motion F_z and following the values of the *z*-component of the band-edge angular momentum J_z. Hence, the 8×8 $\mathbf{k}\cdot\mathbf{p}$ Hamiltonian can be diagonalized in each Hilbert subspace I, II independently in different *M* subspaces.

According to our model, states (1) and (2) should fulfill the boundary condition $\Psi^M_{\mathrm{I,II}}(R)=0$ at the dot radius *R* and, therefore, the wave numbers occurring in each component $f^M_{n,L}(\mathbf{r})$ are given by $k^L_n=\mu^L_n/R$, where μ^L_n is the *n*th zero of $j_L(x)$. Notice yet that each state $\psi^M_{\mathrm{I}}(\mathbf{r})$ or $\psi^M_{\mathrm{II}}(\mathbf{r})$ differs from the usual descriptions which classify them by their parities.[10] The order imposed upon the orbital quantum number *L* in Eqs. (1) and (2) is determined by the off-diagonal elements in the Hamiltonian (A2). The operators $\hat{P}_\pm$ change the parity of angular envelope function $Y^M_L(\theta,\phi)$ while $\hat{P}_z$ preserves the parity of the orbital angular momentum. Both conduction-valence band coupling and the valence-band mixing, appearing as combinations of the operators $\hat{P}_+$, $\hat{P}_-$, and $\hat{P}_z$ in the off-diagonal terms of the Hamiltonian, determine how the states must be constructed. Clearly, the states cannot be classified anymore as symmetric or antisymmetric, as can be done for the parabolic Hamiltonian model or the odd/even classification that has been used for the spherical[9] and for the Pidgeon and Brown Hamiltonian models.[20] The axial approximation, where $\gamma_2 \neq \gamma_3$, couples all carrier components $|e^{\pm}\rangle$, $|hh^{\pm}\rangle$, $|lh^{\pm}\rangle$, $|so^{\pm}\rangle$ and this implies that for a given M all values of the quantum number L, fulfilling the condition $L \geqslant |M|$, have to be taken into account.

Finally we need to mention that the classification of the states in the Hilbert subspaces I, II and independently in different M subspaces simplifies tremendously the calculation (the order of the matrices to be diagonalized is reduced), permits a precise study of the selection rules for the optical transitions, as well as allows an unambiguous analysis of the final results.

(iv) In our matrix diagonalization scheme we have ordered the basis sets $\{f_{n,L}^{M}(\mathbf{r})\}$ for increasing values of the energy eigenvalues E_i, $i=1,\ldots,N$. Therefore, we can replace the sums $\Sigma_{n,L}$, in expansions (1) and (2), by Σ_{E_i}, with fixed value of M. This procedure permits to select only those most important contributions to construct a given spinor. The total number of values of N used can be fixed when an appropriate convergence condition has been reached. In this approach we have diagonalized much smaller matrices than those used in the normally standard procedures, with a consequent gain in the computational efficiency besides discarding many zeros in the matrix to be diagonalized.

(v) The complete Kane-Weiler Hamiltonian (A2) used in this work neglects only the warping terms, proportional to the parameter $\mu=(\gamma_2-\gamma_3)/2$, which appear in the off-diagonal element W [see Eq. (A4)]. In all other components of the Hamiltonian (A2) we have kept $\gamma_2 \neq \gamma_3$, thus preserving its axial nature as well as the type of coupling between the Kramer doublets for each carrier. This asymmetry is reflected in the difference of the contributions from remote conduction bands to the carrier effective masses, γ_2 and γ_3. Note that this difference on the effective masses is neglected if the spherical approximation is considered.

The current growth techniques for quantum dots synthesized in host matrices can produce samples with narrow size distributions ($<5\%$) of nanocrystallites. Uniform shapes have also been obtained besides the high degree of reproducibility and control already reached. Additionally to these technological facts, at the present time, the characterization processes and size selective optical techniques such as fluorescence,[20] low-temperature two-photon fluorescence excitation microscopy[21] and far-field microscopy[22] have permitted to study the optical properties of an isolated quantum dot, confirming the δ-function-like character for its density of states.

B. Selection rules, oscillator strengths, and optical absorption

In the framework of the Pidgeon and Brown Hamiltonian model treating an also spherical central potential, all three Cartesian axes become identical. Besides, any radial direction in the sphere can be taken as the quantization axis in this symmetry and, in principle, any optical selection rules for incident light with linear or circular polarization are equivalent. As we mentioned for the axial Hamiltonian model, there will be some different effective masses along the quantization direction (taken as z axis) and on the plane perpendicular to this (denoted by x-y plane). It is important since for all crystals of interest here, the Γ_8 valence-band states show different effective masses in these two non-equivalent directions according to the p-type character of the hole branches. However, the other two carriers belonging to Γ_6 (s-character) and Γ_7 (p-character) bands are spherical symmetric implying equal curvatures (effective masses) in any direction. We may infer that, at least away from the spherical interface and may be for radii not "too small," the SQD grown by any process should have a lattice with the same bulklike symmetry properties. Therefore, these differences in the carrier and their effective masses should be reflected in the optical experiments. Moreover, it is implied that a proper lattice direction should be identified in a given sample (see for example Ref. 24). In the following we have chosen to assign the proper z-quantization axis along the wave vector of the incident light with circular polarization ($\hat{\mathbf{e}}^{+}$ or $\hat{\mathbf{e}}^{-}$). It is important to remark that in colloidal or host matrix samples, to grow QD's in a certain crystalline direction may become experimentally difficult, depending on the density and on the size of the dots.[24]

Within the present growth progresses, our calculation can neglect the effects of non-homogeneous broadening, which arise from the dot size fluctuations in a sample. Thus, the absorption spectra will be calculated by considering only a constant homogeneous broadening Γ, which may be assigned to the presence of phonons, impurities, surface states, etc. In order to discuss the optical absorption spectrum, the probability for dipole-allowed optical transitions between single electron and hole states has to be evaluated in detail.

Within the electrical dipole approximation, the oscillator strength is a linear combination of the matrix elements of the optical transitions,

$$\langle \psi_j|\hat{\mathbf{e}}\cdot\hat{\mathbf{P}}|\psi_{j'}\rangle=\langle f_j|f_{j'}\rangle\langle u_j|\hat{\mathbf{e}}\cdot\hat{\mathbf{P}}|u_{j'}\rangle+\langle u_j|u_{j'}\rangle\langle f_j|\hat{\mathbf{e}}\cdot\hat{\mathbf{P}}|f_{j'}\rangle. \tag{3}$$

Here, $\hat{\mathbf{e}}$ is the light polarization vector, $\hat{\mathbf{P}}$ is the momentum operator, f_j and u_j are the envelope and periodic Bloch functions at the Γ point for each involved carrier j, respectively. The second term on the right-hand side of Eq. (3) is responsible for intraband optical transitions, since $\langle u_j|u_{j'}\rangle=\delta_{jj'}$. In this case the incident light couples, in the same band, states with different symmetries whenever the term $\langle f_j|\hat{\mathbf{e}}\cdot\hat{\mathbf{P}}|f_{j'}\rangle \neq 0$ for given polarization. These optical transitions correspond to a range of excitation laser energies, $\hbar\omega$ (typically hundreds of meV), smaller than the fundamental gap E_g. In the following we will solely study the first term of Eq. (3) given the contributions for interband transitions, i.e., in the range where $\hbar\omega \gtrsim E_g$. In CdTe the interband and intraband optical transitions are well separated in energies and can be studied independently. We need to remark that if narrow band-gap semiconductors are considered both terms in Eq. (3) have to be considered in the analysis of their optical properties. The interband term can be separated in the integration over the fast oscillating Bloch part, which will determine the interband selection rules between the Bloch states, and the integration over the smooth envelope part determining the intensity of an allowed transition. The integration over the Bloch function results in the size-independent dipole matrix elements that will be named $\Pi_{j,j'}$. In our case the complete set of selection rules are obtained from the nonvanishing products of the matrix elements $I_{e,h}\delta_{L_e,L_h}\Pi_{\alpha,\alpha'}$, where $I_{e,h}=\langle f_{e,\alpha}|f_{h,\alpha'}\rangle$ is the overlap integral of the electron-hole envelope functions allowed by the interband transition $\alpha\rightarrow\alpha'$. The allowed transitions between states belonging to the Hilbert subspaces described by spinors (1) and (2) are determined from the angular dependence of the wave functions $f_{n,L}^{M}(\mathbf{r})$. According to our choice $\hat{\mathbf{z}}\|\boldsymbol{\kappa}$, the interband dipole matrix for incident light with left circular (σ^-) polarization, $\hat{\mathbf{e}}^-=(\mathbf{x}-i\mathbf{y})/\sqrt{2}$, is given by

$$\boldsymbol{\Pi}^-=\frac{iP}{\sqrt{3}}\begin{bmatrix} 0 & -\sqrt{3} & 0 & 0 & 0 & 0 & 0 & 0\\ 0 & 0 & 0 & 0 & 0 & 0 & 0 & 0\\ 0 & 0 & 0 & 0 & 0 & 0 & 0 & 0\\ 0 & 0 & 0 & 0 & 0 & 0 & 0 & 0\\ 0 & 0 & 1 & \sqrt{2} & 0 & 0 & 0 & 0\\ 0 & 0 & 0 & 0 & -\sqrt{3} & 0 & 0 & 0\\ -1 & 0 & 0 & 0 & 0 & 0 & 0 & 0\\ -\sqrt{2} & 0 & 0 & 0 & 0 & 0 & 0 & 0 \end{bmatrix}, \tag{4}$$

where $(iP)=i\langle S|P_x|X\rangle$ is proportional to the Kane coupling parameter P_0. The corresponding matrix interaction σ^+ is obtained from the Hermitian adjoint $\Pi^+=-[\Pi^-]^\dagger$.

On the grounds established by Eq. (4), the corresponding selection rules for each optical transition in any polarization can be precisely obtained. It can be seen, according to the structure of both obtained Hilbert subspaces and the dipole matrices, that only the allowed transitions are those between initial $M_i(H_i)$ and final $M_f(H_f)$ levels belonging to different subspaces $H=\mathrm{I}$, II. This is due to the difference in the angular momenta L (symmetry) of electron and hole components in the subspaces. Moreover, the preservation of the projection of the total angular momentum F_Z ($\Delta F_Z=F_{Ze}-F_{Zh}=0$) requires for the magnetic quantum number that $\Delta M=\pm1$.

For left circular polarization, the optical matrix element (3) takes the form

$$\langle\psi_{e,\mathrm{I}}^{M_e}|\hat{\mathbf{e}}^-\cdot\hat{\mathbf{P}}|\psi_{h,\mathrm{II}}^{M_h}\rangle=iP\mathcal{F}_{N_e,M_e}^{N_h,M_h}(\mathrm{I},\mathrm{II})\,\delta_{M_e,M_h\pm1}, \tag{5}$$

where

$$\mathcal{F}_{N_e,M_e}^{N_h,M_h}(\mathrm{I},\mathrm{II})=\sum_{n,L\geqslant|M|}\left\{-A_{n,\beta}^{e^\pm}A_{n,\beta}^{hh^\pm}\right.$$
$$\left.\pm\frac{1}{\sqrt{3}}A_{n,\beta}^{e^\mp}\left[A_{n,\beta}^{lh^\pm}+\frac{1}{\sqrt{2}}A_{n,\beta}^{so^\pm}\right]\right\}, \tag{6}$$

with $\beta=(2L+1/2\mp1/2)$. In the same way the I→II transitions can be obtained by interchanging $2L+1/2\mp1/2$ by $2L+1/2\pm1/2$. To right circular polarization $\hat{\mathbf{e}}^+$ we solely have to substitute the signs $(\pm)$ in Eqs. (5) and (6) by $(\mp)$ and vice versa.

In order to discuss the optical absorption spectra, the interband oscillator strength $|\mathcal{F}|^2$ between single electron (N_e,M_e) and hole (N_h,M_h) states has to be evaluated. The absorption coefficient can then be written as

$$\alpha(\hat{\mathbf{e}}^-,\omega)=\alpha_0\sum_{N_e,N_h,M}\frac{\Gamma}{\pi}$$
$$\times\left\{\frac{|\mathcal{F}_{N_e,M}^{N_h,M\pm1}(\mathrm{I},\mathrm{II})|^2}{[E_{N_e,M}(\mathrm{I})-E_{N_h,M\pm1}(\mathrm{II})-\hbar\omega]^2+\Gamma^2}\right.$$
$$\left.+\frac{|\mathcal{F}_{N_e,M}^{N_h,M\mp1}(\mathrm{II},\mathrm{I})|^2}{[E_{N_e,M}(\mathrm{II})-E_{N_h,M\mp1}(\mathrm{I})-\hbar\omega]^2+\Gamma^2}\right\}, \tag{7}$$

where α_0 is a magnitude which includes the bulk P parameter, the dielectric constant, etc. As we have pointed out in the Introduction the warping term μ was neglected, providing an 8×8 $\mathbf{k}\cdot\mathbf{p}$ Hamiltonian with cylindrical symmetry. In CdSe $\gamma_2\approx\gamma_3$ and the warping term contribution to the quasiparticle energies and optical selection rules can be ruled by perturbation theory. In this case other electronic transitions have to be added, for example to Eq. (6). Nevertheless and since the corresponding oscillator strength is proportional to the μ parameter, these new contributions to the optical spectrum are smaller, in comparison with those obtained through Eq. (6), in the cylindrical approximation.

III. RESULTS

The parameters for CdTe (Ref. 10) used in this calculation are the energy band gap $E_g=1.6069$ eV, the spin-orbit energy $\Delta_0=0.953$ eV. The Luttinger parameters $\gamma_1^L=5.37$, $\gamma_2^L=1.67$, $\gamma_3^L=1.98$, the nonparabolicity for the conduction band $(1+2F)=1.24$, the electron effective mass $m_e=0.091m_0$, and the Kane conduction-valence band coupling $E_p=17.9$ eV. For all calculated optical spectra in this work we have used a unique value for the homogeneous electronic broadening, $\Gamma=20$ meV.

For the numerical calculation we have built each M subspace using as basis all the possible electronic states that fulfill the condition $E\leqslant2.5$ eV. Hence, the results we present can achieved using matrices of size of $8N_0\times8N_0$, with $N_0\leqslant30$.

In Fig. 1 we show the variation of the first electron and hole energy levels as a function of $1/R^2$. We identify the levels by the magnetic quantum number M and by the index $n=1,2\ldots$ that enumerates the ordering of levels by increasing values of the energy. Thus, the electron (hole) levels are

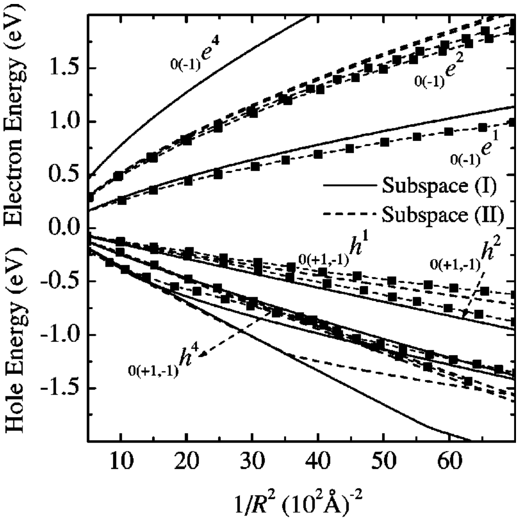

FIG. 1. Electron and hole energy spectra of a CdTe SQD as calculated in Sec. II A, plotted the inverse-mean-square radius $1/R^2$. Solid (dashed) lines represent states arising from the Hilbert subspace I (II). Some levels have been identified considering the quantum number M and the energy ordering index n (see text for details). Square-dashed lines indicate the same result according to the spherical approximation.

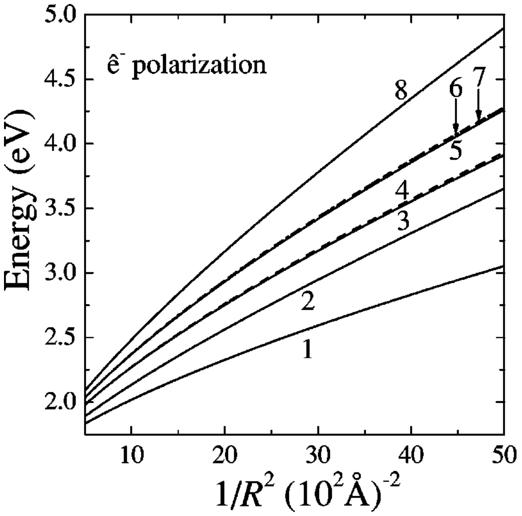

FIG. 2. Transition energies obtained from the $\mathbf{k}\cdot\mathbf{p}$ model for $\hat{\mathbf{e}}^{-}$ polarization for a CdTe SQD. The numbers indicate the following transitions: 1, ${}_{0(-1)}e^1(\mathrm{I})\leftarrow{}_{1,(0)}h^1(\mathrm{II})$; 2, ${}_{0(-1)}e^1(\mathrm{I})\leftarrow{}_{1,(0)}h^2(\mathrm{II})$; 3, ${}_{0(-1)}e^1(\mathrm{II})\leftarrow{}_{1,(0)}h^1(\mathrm{I})$; 4, ${}_{0(-1)}e^1(\mathrm{II})\leftarrow{}_{1,(0)}h^2(\mathrm{I})$; 5, ${}_{0(-1)}e^2(\mathrm{II})\leftarrow{}_{1,(0)}h^1(\mathrm{I})$; 6, ${}_{0(-1)}e^2(\mathrm{II})\leftarrow{}_{1,(0)}h^2(\mathrm{I})$; 7, ${}_{1(-2)}e^1(\mathrm{II})\leftarrow{}_{2,(-1)}h^1(\mathrm{I})$; 8, ${}_{1(-2)}e^1(\mathrm{II})\leftarrow{}_{2,(-1)}h^2(\mathrm{I})$. Transitions 4 and 6, 7 are labeled by dashed lines and line dots, respectively.

labeled in the following way: ${}_{M}e^{n}(H)[{}_{M}h^{n}(H)]$, and $H=\mathrm{I,II}$ representing which Hilbert subspace the carrier state belongs to. This notation is appropriate if we consider the form in which each state function [Eqs. (1) and (2)] is written. Our diagonalization scheme has allowed an easy identification of the levels as well as the optical transitions. The level degeneracy is indicated in the figure by parentheses, that is, ${}_{0(-1)}e^1(\mathrm{I})$ meaning that the state is doubly degenerate for the values of $M=\{0,-1\}$. Due to the full confinement, the average spacing between levels increases with decreasing values of R. The figure shows clearly the existence of nonparabolicity in the conduction-band levels and the effects of the admixture between heavy and light holes resulting in the anticrossing at $R\approx 13$ Å. It will be very useful to check the differences between the calculated electronic states by using the spherical model or the axial approximation. A direct comparison is given in Fig. 1 where the data of Ref. 10 are shown by square-dashed lines. The energy values of Ref. 10 are well reproduced by our calculations when the approximation of $\gamma_2=\gamma_3$ is considered and the same set of parameters are used for CdTe.

It can be seen that the eigenenergy values for the conduction band in both models are nearly the same. Nevertheless, the difference increases as the SQD radius decreases. For example the level ${}_{0(-1)}e^1(\mathrm{I})$ in both approximations presents a difference of 140 meV at $R=13$ Å. The same we can argue with respect to the valence band for the first two heavy-hole states: ${}_{0}h^1(\mathrm{II})$ and ${}_{0}h^2(\mathrm{II})$. A more significative behavior (quantitative and qualitative) can be observed for the other hole excited states at any value of the QD radius. These differences have their origin in the Hamiltonians. It is seen that electron- and heavy-hole states are less influenced (only numerically through their effective masses) by the axial component inherent in the zinc-blende symmetry of many II-VI and III-V based semiconductor nanostructures. Thus, the energies of the first light-hole and of the other excited states [except the ${}_{0}h^2(\mathrm{II})$] in the valence band are strongly modified by the presence of the axial components ($\gamma_2\neq\gamma_3$) in comparison to those calculated with a complete spherical QD Hamiltonian. Another interesting feature in Fig. 1 is the observed splitting in the conduction band [state ${}_{0(-1)}e^2(\mathrm{II})$ shown by dashed lines] and also in the valence band [state ${}_{0(-1)}h^4(\mathrm{II})$ shown by dashed lines]. The main reason for these splittings is the existing coupling between electron- and light-hole states, a first-order contribution generated by the linear terms proportional to $\hat{K}_{-}$ in Eq. (A2). Also, these matrix element coupling blocks with different spin orientations break their Kramer doublets degeneracy. We can see that the same behavior is obtained in Ref. 10 for the electron but complete different values for hole level energy are found for the spherical model.

Figure 2 shows the calculated interband transition energies ΔE as a function of the inverse of the square of the SQD radius. Notice that for dot sizes below 100 Å, the nonlinear shape of the transition energies also reveals the strong nonparabolicity and the inherent multiple band mixture effects. It is important to remark that the linear approach $\Delta E=a+b/R^2$, as used in some works[25] to interpret the optical properties, can be applied only for a very limited range of dot sizes.

According to our notation, an interband transition from the initial hole state, characterized by quantum numbers (n_i, M_i) , to the final electron state defined by (n_f, M_f) is represented as ${}_{M_f}e^{n_f}(\mathrm{H}_f)\leftarrow{}_{M_f}h^{n_i}(\mathrm{H}_i)$. In this calculation, we

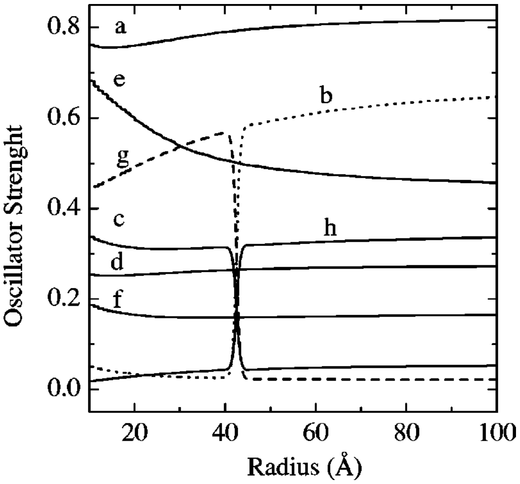

FIG. 3. Calculated oscillator strength as a function of the SQD radius, in left circular $\hat{\mathbf{e}}^-$ polarization. The shown transitions are as follows: ${}_0e^1(\mathrm{I})\leftarrow {}_1h^1(\mathrm{II})$; $b, {}_0e^1(\mathrm{II})\leftarrow {}_1h^1(\mathrm{I})$; c: ${}_{-1}e^1(\mathrm{II})\leftarrow {}_0h^1(\mathrm{I})$; $d, {}_{-1}e^1(\mathrm{I})\leftarrow {}_0h^1(\mathrm{II})$; $e, {}_1e^1(\mathrm{II})\leftarrow {}_2h^1(\mathrm{I})$; $f, {}_{-2}e^1(\mathrm{II})\leftarrow {}_{-1}h^1(\mathrm{I})$, $g, {}_0e^2(\mathrm{II})\leftarrow {}_1h^1(\mathrm{I})$; $h, {}_{-1}e^2(\mathrm{II})\leftarrow {}_0h^1(\mathrm{I})$.

have neglected any effect of temperature by assuming that the carrier Fermi occupations are $F(E_c)\approx 1$ and $F(E_v)\approx 0$.

In Fig. 3 we present the calculated oscillator strengths as a function of R, in a CdTe SQD, for circular $\hat{\mathbf{e}}^-$ polarization. The involved transitions were obtained from the general interband selection rule $\Delta M=\pm 1$ as can be identified in the figure.

Two qualitative characteristics can be observed in Fig. 3:(i) The strongest contributions are transitions starting in the first hole state, (ii) the oscillator strength presents a general slow variation with the dot radius. For some specific transitions and for well defined dot radius, the oscillator strength shows a very sharp variation. For example, in Fig. 3 a clear interchange of optical strengths between the transitions c and g can be observed at approximately $R=42$ Å. For dot sizes $R<42$ Å the transition g is the dominant one while that labeled as c is extremely weak. Just the opposite happens for $R>42$ Å where the transition c becomes the dominant one. These facts can be understood by considering that the final states of the mentioned transitions are ${}_0e^1(\mathrm{II})$ and ${}_0e^2(\mathrm{II})$, or the levels that present the anticrossing effect near $R=42$ Å. At this value the states are interchanging their character and, according to selection rules, the oscillator strength will display the character of the most favored transition.

Figure 4 shows the calculated optical absorption spectra for the $\hat{\mathbf{e}}^-$ polarization in SQD with $R=30$ Å and $R=50$ Å. Due to symmetry arguments, the shape of the absorption profile for $\hat{\mathbf{e}}^+$ must be exactly the same as for $\hat{\mathbf{e}}^-$ polarization. This fact is a consequence of the spatial symmetry of the system that assures that the involved states must have degenerate energy levels with respect to quantum number M. Obviously, any deviation from the present symmetry, as induced by electric or magnetic fields or by shape deformation, can break the $2L+1$ degeneracy of M, producing significant differences between $\hat{\mathbf{e}}^+$, $\hat{\mathbf{e}}^-$ absorption spectra.

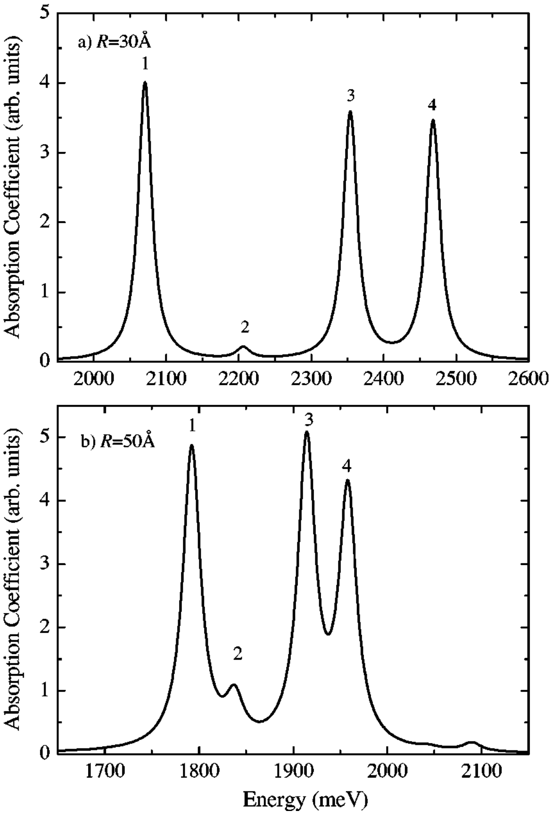

FIG. 4. Absorption spectra for $\hat{\mathbf{e}}^-$ polarization in CdTe SQD with $R=30$ Å and 50 Å. Peaks contributing to the optical absorption are as follows: 1, ${}_0e^1(\mathrm{I})\leftarrow {}_1h^1(\mathrm{II})$, ${}_{-1}e^1(\mathrm{I})\leftarrow {}_0h^1(\mathrm{II})$; 2, ${}_0e^1(\mathrm{I})\leftarrow {}_1h^2(\mathrm{II})$, ${}_{-1}e^1(\mathrm{I})\leftarrow {}_0h^2(\mathrm{II})$; 3, ${}_0e^1(\mathrm{II})\leftarrow {}_1h^1(\mathrm{I})$, ${}_0e^2(\mathrm{II})\leftarrow {}_1h^1(\mathrm{I})$, ${}_{-2}e^1(\mathrm{II})\leftarrow {}_{-1}h^1(\mathrm{I})$, ${}_{-1}e^1(\mathrm{II})\leftarrow {}_0h^1(\mathrm{I})$, ${}_{-1}e^2(\mathrm{II})\leftarrow {}_0h^1(\mathrm{I})$; 4, ${}_0e^1(\mathrm{II})\leftarrow {}_1h^2(\mathrm{I})$, ${}_0e^2(\mathrm{II})\leftarrow {}_1h^2(\mathrm{I})$, ${}_1e^1(\mathrm{II})\leftarrow {}_2h^1(\mathrm{I})$, ${}_1e^1(\mathrm{II})\leftarrow {}_2h^2(\mathrm{I})$, ${}_{-2}e^1(\mathrm{II})\leftarrow {}_{-1}h^2(\mathrm{I})$, ${}_{-1}e^1(\mathrm{II})\leftarrow {}_0h^2(\mathrm{I})$, ${}_{-1}e^2(\mathrm{II})\leftarrow {}_0h^2(\mathrm{I})$.

The overall absorption profile shown in Fig. 4 is a result of the addition of all 16 possible contributions which are listed in the caption of the figure. Some contributions to the peaks 3 and 4 are slightly shifted from each other, since they arise from very close but not degenerate energy levels, as can be seen in Figs. 1 and 2. This difference is sufficiently small so that when the separate contributions are added the resulting profile (solid line) shows only one peak due to the large value for the broadening used in the present calculation. To resolve spectroscopically these contributions we would need a smaller value for the phenomenological linewidth Γ, a possibility that could only be checked from the experiments done in high quality samples.

It is completely clear that both mentioned Hamiltonian models will present different characteristic behavior for the optical properties, in particular, for those transitions involving electron and hole excited states. Another experimental evidence that seems interesting is the possibility to distinguish interband spectra from the two Hamiltonian models described before, a fact that would demand optical experiments using different independent polarizations of incident light on the same SQD.

IV. CONCLUSIONS

Within the framework of the **k·p** multiband effective-mass approximation we have studied the main features concerning to the electronic structure and the optical properties for SQD's in the regime of strong confinement. The results obtained in our calculation for the eigenstates and eigenvalues have shown the relevant aspects of interlevel coupling on the study of the optical and electronic properties. The Hilbert space of solutions and their symmetry properties for the 8×8 **k·p** Hamiltonian were deeply analyzed providing a detailed study of the optical properties and their dependence on the dot size and SQD parameters. The nonhomogeneous effects of the size distribution have been neglected and the light-matter interaction was addressed in the dipole approximation. Also, we have shown that the two types of **k·p** Hamiltonians, spherical and axial models, will conduce to different hole energy dispersions and different optical transitions. It has been clarified that as long as γ_2 is not equal to γ_3 both models provide different values of the electron and hole energy spectra. Our results are the starting steps for a complete and rigorous discussion of other optical properties in semiconductor quantum dots and possibility to observe different polarization excitations. The present results are completely valid for any other SQD nanostructure as CdS, CdSe, etc.

ACKNOWLEDGMENTS

This work was supported by Fundação de Amparo à Pesquisa do Estado de São Paulo (FAPESP) and by Conselho Nacional de Desenvolvimento Científico e Tecnológico (CNPq).

APPENDIX: THE 8×8 k·p HAMILTONIAN

Some details of the conventional **k·p** formalism used in this work are shown. We define the basis states $|J,J_z\rangle$ in terms of spin and orbital wave functions with *s*-type symmetry for the two conduction bands (e), and those with *p*-type symmetry for the six valence bands, corresponding to heavy (hh), light (lh) and spin-orbit (so) holes. They are represented by

$$
\begin{aligned}
|e^+\rangle &= |\tfrac{1}{2},\tfrac{1}{2}\rangle = |s\uparrow\rangle,\\
|hh^+\rangle &= |\tfrac{3}{2},\tfrac{3}{2}\rangle = -i\sqrt{\tfrac{1}{2}}|(x+iy)\uparrow\rangle,\\
|lh^+\rangle &= |\tfrac{3}{2},\tfrac{1}{2}\rangle = -i\sqrt{\tfrac{1}{6}}[|(x+iy)\downarrow\rangle - 2|z\uparrow\rangle],\\
|so^+\rangle &= |\tfrac{1}{2},\tfrac{1}{2}\rangle = -i\sqrt{\tfrac{1}{3}}[|(x+iy)\downarrow\rangle + |z\uparrow\rangle],\\
|e^-\rangle &= |\tfrac{1}{2},-\tfrac{1}{2}\rangle = |s\downarrow\rangle,\\
|hh^-\rangle &= |\tfrac{3}{2},-\tfrac{3}{2}\rangle = -i\sqrt{\tfrac{1}{2}}|(x-iy)\downarrow\rangle,\\
|lh^-\rangle &= |\tfrac{3}{2},-\tfrac{1}{2}\rangle = i\sqrt{\tfrac{1}{6}}[|(x-iy)\uparrow\rangle + 2|z\downarrow\rangle],\\
|so^-\rangle &= |\tfrac{1}{2},-\tfrac{1}{2}\rangle = i\sqrt{\tfrac{1}{3}}[|(x-iy)\uparrow\rangle - |z\downarrow\rangle]. \qquad \text{(A1)}
\end{aligned}
$$

Notice that we have used a different ordering of the band-edge Bloch states. In the above sequence of states, the Hamiltonian matrix takes the form given below, after Kane[16] and Weiler,[18] and represents the kinetic energy of the carriers:

$$
H_{\mathbf{k}\cdot\mathbf{p}} = \begin{bmatrix}
\hat{D}_{el} & -\sqrt{3}\hat{K}_+ & \sqrt{2}\hat{K}_z & -\hat{K}_z & 0 & 0 & \hat{K}_- & \sqrt{2}\hat{K}_- \\
 & \hat{D}_{hh} & -\hat{G}_- & \frac{1}{\sqrt{2}}\hat{G}_- & 0 & 0 & -\frac{1}{2}\hat{W} & -\frac{1}{\sqrt{2}}\hat{W} \\
 & & \hat{D}_{lh} & \hat{R} & -\hat{K}_- & \frac{1}{2}\hat{W} & 0 & \sqrt{\frac{3}{2}}\hat{G}_- \\
 & & & \hat{D}_{so} & -\sqrt{2}\hat{K}_- & \frac{1}{\sqrt{2}}\hat{W} & -\sqrt{\frac{3}{2}}\hat{G}_- & 0 \\
 & & & & \hat{D}_{el} & -\sqrt{3}\hat{K}_- & \sqrt{2}\hat{K}_z & -\hat{K}_z \\
 & & & & & \hat{D}_{hh} & -\hat{G}_+ & \frac{1}{\sqrt{2}}\hat{G}_+ \\
 & & & & & & \hat{D}_{lh} & \hat{R} \\
 & & & & & & & \hat{D}_{so}
\end{bmatrix}. \qquad \text{(A2)}
$$

Each diagonal element is defined as

$$\hat{D}_{el}=E_g+(F+1/2)\hat{\mathbf{P}}^2,$$

$$\hat{D}_{hh}=\hat{D}_+,$$

$$\hat{D}_{lh}=\hat{D}_-, \tag{A3}$$

$$\hat{D}_\pm=\left(\frac{\gamma_1\pm\gamma_2}{2}\right)\hat{\mathbf{P}}^2\mp\frac{3}{2}\gamma_2\hat{P}_z^2,$$

$$\hat{D}_{so}=-\Delta_0+\frac{\gamma_1}{2}\hat{\mathbf{P}}^2.$$

The off-diagonal terms are given by

$$\hat{K}_\pm=iP_0\sqrt{\frac{1}{6}}\hat{P}_\pm, \tag{A4}$$

$$\hat{G}_\pm=\sqrt{3}\gamma_3\hat{P}_\pm\hat{P}_z,$$

$$\hat{K}_z=iP_0\sqrt{\frac{1}{3}}\hat{P}_z,$$

$$\hat{W}=\sqrt{3}(\overline{\gamma}\hat{P}_-^2-\mu\hat{P}_+^2),$$

$$\hat{R}=\frac{\sqrt{2}}{2}\gamma_2(\hat{\mathbf{P}}^2-3\hat{P}_z^2).$$

In the above expressions, we define the momentum operators as $\hat{P}_\pm=[\partial/\partial x\pm i(\partial/\partial y]$, $\hat{P}_z=\partial/\partial z$ and $\hat{\mathbf{P}}^2=\nabla^2$. The additional parameters are given by

$$\overline{\gamma}=\tfrac{1}{2}(\gamma_2+\gamma_3),$$

$$\mu=\tfrac{1}{2}(\gamma_2-\gamma_3).$$

The second-order parameters F, γ_1, γ_2, and γ_3 take into account the contributions of the remote bands to the conduction (electron) and valence (holes) effective masses, respectively and are measured in units of $\hbar^2/m_0$. Finally $P_0=i(\hbar/m_0)\langle s|p_x|x\rangle$ is the usual first-order Kane parameter (measured in meV Å) or $E_p=(2m_0/\hbar^2)P_0^2$ (meV) which sets the strength of the conduction-valence band coupling. Writing the operators $\hat{P}_\pm$ and $\hat{P}_z$ in spherical coordinates and using the wave function $f_{n,L}^M(r,\Omega)$ introduced in Sec. II, the off-diagonal matrix elements are given by

$$\langle f_{n',L'}^{M'}|\hat{P}_+|f_{n,L}^M\rangle =2k_n^L\delta_{M',M+1}I_{L',L}^{n',n}[\delta_{L',L+1}b_{L,M}-\delta_{L',L-1}c_{L,M}], \tag{A5}$$

$$\langle f_{n',L'}^{M'}|\hat{P}_-|f_{n,L}^M\rangle=2k_n^L\delta_{M',M-1}I_{L',L}^{n',n}[-c_{L+1,M-1}\delta_{L',L+1} +b_{L-1,M-1}\delta_{L',L-1}], \tag{A6}$$

$$\langle f_{n',L'}^{M'}|\hat{P}_z|f_{n,L}^M\rangle =2k_n^L\delta_{M',M}I_{L',L}^{n',n}[-a_{L+1,M}\delta_{L',L+1}-a_{L,M}\delta_{L',L-1}], \tag{A7}$$

$$\langle f_{n',L'}^{M'}|\hat{P}_-^2|f_{n,L}^M\rangle=2(k_n^L)^2\delta_{M',M-2}I_{L',L}^{n',n}\times\left[\delta_{L',L+2}\left(\frac{2L+3}{\mu_n^L}\right)c_{L+2,M-2}c_{L+1,M-1}-\delta_{L',L-2}\left(\frac{2L-1}{\mu_n^L}\right)b_{L-2,M-2}b_{L-1,M-1}\right], \tag{A8}$$

$$\langle f_{n',L'}^{M'}|\hat{P}_+^2|f_{n,L}^M\rangle=2(k_n^L)^2\delta_{M',M+2}I_{L',L}^{n',n}\times\left[\delta_{L',L+2}\left(\frac{2L+3}{\mu_n^L}\right)b_{L,M}b_{L+1,M+1}+\delta_{L',L-2}\left(\frac{2L-1}{\mu_n^L}\right)c_{L,M}c_{L-1,M+1}\right], \tag{A9}$$

$$\langle f_{n',L'}^{M'}|\hat{P}_z^2|f_{n,L}^M\rangle=2(k_n^L)^2\delta_{M',M}I_{L',L}^{n',n}\times\left[\delta_{L',L+2}\left(\frac{2L+3}{\mu_n^L}\right)a_{L+1,M}a_{L+2,M}-\delta_{L',L-2}\left(\frac{2L-1}{\mu_n^L}\right)a_{L-1,M}a_{L,M}\right], \tag{A10}$$

$$\langle f_{n',L'}^{M'}|\hat{P}_+\hat{P}_z|f_{n,L}^M\rangle=-2(k_n^L)^2\delta_{M',M+1}I_{L',L}^{n',n}\times\left[\delta_{L',L+2}\left(\frac{2L+3}{\mu_n^L}\right)a_{L+1,M}b_{L+1,M}+\delta_{L',L-2}\left(\frac{2L-1}{\mu_n^L}\right)c_{L-1,M}a_{L,M}\right], \tag{A11}$$

$$\langle f_{n',L'}^{M'}|\hat{P}_-\hat{P}_z|f_{n,L}^M\rangle=2(k_n^L)^2\delta_{M',M-1}I_{L',L}^{n',n}\times\left[\delta_{L',L+2}\left(\frac{2L+3}{\mu_n^L}\right)a_{L+1,M}c_{L+2,M-1}+\delta_{L',L-2}\left(\frac{2L-1}{\mu_n^L}\right)b_{L-2,M_{-1}}a_{L,M}\right], \tag{A12}$$

where

$$a_{L+1,M}=\sqrt{\frac{(L-M+1)(L+M+1)}{(2L+1)(2L+3)}},$$

$$b_{L,M}=\sqrt{\frac{(L+M+2)(L+M+1)}{(2L+1)(2L+3)}}, \tag{A13}$$

$$c_{L,M}=\sqrt{\frac{(L-M)(L-M-1)}{(2L-1)(2L+1)}},$$

and the overlap integrals are

$$I_{L',L}^{n',n}=\frac{\mu_{n'}^{L'}}{(\mu_{n'}^{L'})^2-(\mu_n^L)^2}.$$

---

*Electronic address: psprado@df.ufscar.br

[1] D.J. Norris and M.G. Bawendi, Phys. Rev. B **53**, 16 338 (1996).

[2] D.J. Norris, A.L. Efros, M. Rosen, and M.G. Bawendi, Phys. Rev. B **53**, 16 347 (1996).

[3] Y. Masumoto and K. Sonobe, Phys. Rev. B **56**, 9734 (1997).

[4] U. Woggon, *Optical Properties of Semiconductor Quantum Dots* (Springer-Verlag, Berlin, 1997).

[5] Y. Masumoto and S. Ogasawara, J. Lumin. **87–89**, 360 (2000).

[6] A.M. de Paula, C.R.M. de Oliveira, G.E. Marques, A.M. Cohen, R.D. Feldman, R.F. Austin, M.N. Islam, and C.L. Cesar, Phys. Rev. B **59**, 10 158 (1999).

[7] A.C.R. Bittencourt, A.M. Cohen, and G.E. Marques, Phys. Rev. B **57**, 4525 (1998).

[8] V. López-Richard, G.E. Marques, and C. Trallero-Giner, Solid State Commun. **114**, 649 (2000).

[9] V. López-Richard, G.E. Marques, C. Trallero-Giner, and J. Drake, Phys. Rev. B **58**, 16 136 (1998).

[10] A.L. Efros and M. Rosen, Phys. Rev. B **58**, 7120 (1998).

[11] H. Fu, L.-W. Wang, and A. Zunger, Phys. Rev. B **57**, 9971 (1998).

[12] J. Li and J. Xia, Phys. Rev. B **61**, 15 880 (2000).

[13] P.C. Sercel and K.J. Vahala, Phys. Rev. B **42**, 3690 (1990).

[14] L.W. Wang, A.J. Williamson, A. Zunger, H. Jiang, and J. Singh, Appl. Phys. Lett. **76**, 339 (2000).

[15] J.B. Xia and J. Li, Phys. Rev. B **60**, 11 540 (1999).

[16] E.O. Kane, J. Phys. Chem. Solids **1**, 249 (1957).

[17] V. López-Richard, Ph.D. thesis, Departamento de Física, Universidade Federal de São Carlos, 2001.

[18] M. H. Weiler, *Magnetooptical Properties of* $Hg_{1-x}Cd_xTe$ *Alloys*, 1st ed., *Semiconductor and Semimetals* Vol. 16 (Academic Press, New York, 1981), Chap. 3, pp. 119–191.

[19] $A_{n,L}=\sqrt{2/R^3}(1/[j_{L+1}(\mu_n^L)])$ is the normalization constant, j_L is the L-order spherical Bessel function, and Y_L^M are the spherical harmonics. The boundary condition determines the value of the numbers μ_n^L.

[20] C.R. Pidgeon and R.N. Brown, Phys. Rev. **146**, 575 (1966).

[21] R.G. Neuhauser, K.T. Shimizu, W.K. Woo, S.A. Empedocles, and M.G. Bawendi, Phys. Rev. Lett. **85**, 3301 (2000).

[22] S.A. Blanton, M.A. Hines, and P. Guyot-Sionnesta, Appl. Phys. Lett. **69**, 3905 (1996).

[23] S.A. Empedocles, D.J. Norris, and M.G. Bawendi, Phys. Rev. Lett. **77**, 3873 (1996).

[24] A. Mews, A.V. Kadavanich, U. Banin, and A.P. Alivisatos, Phys. Rev. B **53**, R13 242 (1996).

[25] M.L. Redigolo, W.A. Arellano, L.C. Barbosa, C.H. Brito Cruz, C.L. Cesar, and A.M. de Paula, Semicond. Sci. Technol. **14**, 58 (1999).